Annual cycle of aerosol direct radiative effect over southeast Italy and sensitivity studies

Anna Maria Tafuro,[1] Stefan Kinne,[2] Ferdinando De Tomasi,[1] and Maria Rita Perrone[1]

Received 20 November 2006; revised 22 May 2007; accepted 5 June 2007; published 17 October 2007.

[1] Aerosol direct radiative effect (DRE) calculations are presented to illustrate the annual cycle of the aerosol impact on the radiative energy balance of the Earth-atmosphere system over southeast Italy. Meteorological parameters from radiosondes, aerosol vertical profiles by lidar, aerosol optical and microphysical properties by ground-based Sun/sky photometry and satellite (MODIS) derived data of solar surface albedo, all referring to the 2003–2004 years, constitute the necessary input to radiative transfer simulations. The monthly evolution of both the solar and infrared aerosol direct radiative effect is examined at the top of the atmosphere (ToA), within the atmosphere and at the Earth's surface. Aside from cloud-free conditions (clear-sky), all-sky conditions are also addressed by adopting ISCCP monthly products. Model results reveal a strong seasonality of the solar aerosol DRE for southeast Italy, which is mainly driven by the available sunlight, but it is also modulated by variations in aerosol properties. Under cloud-free conditions, winter aerosol DREs are within $-(6 \pm 2)$ W/m^2 at the ToA and $-(7 \pm 2)$ W/m^2 at the surface, while summer aerosol DREs are within $-(9 \pm 1)$ W/m^2 at the ToA and $-(15 \pm 3)$ W/m^2 at the surface. The larger difference in summer indicates that the heating of the aerosol layer (atmospheric forcing) is much stronger in summer and actually largest in early fall. Under all-sky conditions the solar aerosol direct radiative effect decreases to $-(4 \pm 1)$ W/m^2 and $-(3 \pm 1)$ W/m^2 in winter and to $-(12 \pm 3)$ W/m^2 and $-(7 \pm 1)$ W/m^2 in summer, at surface and ToA, respectively. Model results also reveal that solar aerosol DREs dominates infrared aerosol DREs. The performed sensitivity studies demonstrate the relatively weak impact of meteorological parameters and aerosol vertical profiles and the strong impact of solar surface albedo values. Finally, it is shown that the simulated all-sky aerosol DRE at the surface is consistent with radiometer measurements.

Citation: Tafuro, A. M., S. Kinne, F. De Tomasi, and M. R. Perrone (2007), Annual cycle of aerosol direct radiative effect over southeast Italy and sensitivity studies, *J. Geophys. Res.*, *112*, D20202, doi:10.1029/2006JD008265.

1. Introduction

[2] Several studies have shown that both natural and anthropogenic aerosols have important effects on the climate of the Earth-atmosphere system [e.g., *Haywood and Shine*, 1997]. Aerosol particles affect the climate directly by scattering and absorbing solar radiation and indirectly by modifying cloud microphysical properties. However, as a consequence of their high spatial and temporal variability, these effects are strongly regional in magnitude and sign [*Nakajima et al.*, 2003]. Thus an overall (annual, global) quantification of the aerosol impact on the Earth's radiative balance is highly uncertain. With the need for accurate data on aerosol and environmental properties, multiple-measurement approaches have been designed to better quantify aerosol impacts on climate, at least on a regional basis. The approaches seek to combine satellite observations, continued observations from ground networks, and data from dedicated field experiments [e.g., *Kaufman et al.*, 2002].

[3] Satellite remote sensing provides samples of aerosol (and environmental properties) patterns on a global scale. Particularly useful are the data of newer generation sensors, such as the Moderate Resolution Imaging Spectroradiometer (MODIS) onboard NASA's Earth Observing System [e.g., *King et al.*, 1992]. However, satellite retrieved properties are often uncertain because of necessary a priori assumptions, in particular over continents. Thus ground-based radiometer networks have been established to provide quality reference points. For instance, the Aerosol Robotic Network (AERONET), a federated network of more than 200 automatic Sun/sky radiometers worldwide [*Holben et al.*, 1998] has been established to get aerosol optical thicknesses (AOT) and other aerosol columnar properties. The European Aerosol Research Lidar Network (EARLINET), consisting of 22 lidar stations in Europe [e.g., *Bösenberg et al.*, 2003; *Matthias et al.*, 2004; *Guibert et al.*, 2005] has instead

[1]Dipartimento di Fisica, Università del Salento, Lecce, Italy.
[2]Max Planck Institute für Meteorologie, Hamburg, Germany.

0148-0227/07/2006JD008265

been established to retrieve aerosol vertical profiles all over Europe.

[4] The interest on local aerosol properties and forcings has challenged new efforts to quantify more accurately at least the regional impact of aerosols on the radiative energy balance. Here, the Mediterranean basin is of particular interest, because significant aerosol loads from urban pollution, biomass burning, and advected mineral dust (during almost cloud-free conditions in summer) have led to one of the largest regional ToA energy losses worldwide [e.g., *Haywood and Boucher*, 2000; *Lelieveld et al.*, 2002; *Andreae et al.*, 2002]. Radiative transfer simulations have been conducted in this study using data from measurements near Lecce (40.33°N, 18.10°E) in southeast Italy, to investigate the aerosol impact and its seasonality in this place of the Mediterranean basin that we believe, can be considered representative of many coastal sites of the central-east Mediterranean. In fact, aerosols have been monitored at a site away from large cities and/or large industrial area, which is on the flat Salento peninsula, at about 20 km from the Adriatic and the Ionian Sea, respectively. Input data include monthly statistics of local aerosol column properties (AERONET), local aerosol vertical distributions (EARLINET), nearby atmospheric profiles (radiosonde data), regional data on solar surface albedo from space sensors (MODIS), and cloud properties (ISCCP).

[5] Section 2 introduces the methodology along with the radiative transfer model and input data. The results for the broadband solar and infrared aerosol direct radiative effect (DRE) under clear-sky and all-sky conditions are presented in section 3. The results on the aerosol DRE sensitivity to surface albedo, aerosol vertical profiles and meteorological profiles are reported in section 4. Simulated net fluxes at the surface are compared to actual measurements in section 5 to support the appropriateness of model input and output data. Concluding remarks are presented in section 6.

2. Two-Stream Model and Input Data

[6] The aerosol direct radiative effect is determined from the difference of two simulations: one with background conditions (e.g., no aerosol) and one with aerosol actual levels. The imposed changes to the radiative energy balance quantify the aerosol direct radiative effect. In this study radiative fluxes for the solar (0.3–3.5 μm) and infrared (4–80 μm) spectral region are determined with a two-stream method using a delta-function scattering approach [e.g., *Meador and Weaver*, 1980]. The simplified method and the simplified relationship for describing the angular distribution of the scattered radiation introduce small errors for the derived forcings. These errors are larger for the larger aerosol sizes and the errors differ in magnitude and sign with the Sun elevation [e.g., *Boucher*, 1998]. In the context of daily averages, however, the overall error is expected to stay below 10%. Eight solar and twelve infrared subbands are considered to properly account for the spectral dependence of atmospheric particle properties: the optical properties (extinction, single-scattering albedo and asymmetry factor) of the atmospheric particles remain constant in each of the 20 subbands. Absorption of trace gases (H_2O, O_3, CO_2, CO, N_2O, and CH_4) is represented by l exponential terms in each of the 20 spectral subbands, with l varying within the 1–12 range. Thus 20 applications of the radiative transfer model are required to account for the solar and infrared spectral dependence of each trace gas. The atmospheric gas absorption coefficients are based on the Lowtran 5 database, which underestimates near-infrared water vapor absorption by about 10% [*Halthore et al.*, 2005]. This deficiency, however, is not expected to have any major influence on the simulated aerosol direct radiative effect, since the aerosol impact is strongest in the UV/visible region of the solar spectrum and since the aerosol DRE is determined from the difference of two simulations. Twenty homogeneous plane-parallel atmospheric layers are used to account for the changes with altitude of the atmospheric parameters and components (e.g., pressure, temperature, particle distributions). With a focus on (lower) tropospheric aerosols, 10 layers (of 500 m thickness each) are placed below 5 km altitude. Radiative fluxes are calculated at the boundaries of the homogeneous plane-parallel layers. In order to account for the diurnal Sun elevation changes, solar radiative transfer simulations are performed at different Sun elevations, assuming, for each month, a characteristic Sun height above the horizon. All available data are then properly weighted to get daily averaged solar radiative fluxes.

[7] To perform a test on the appropriateness of model input and output data, broadband shortwave irradiance components computed by this model for two standard atmospheres [*Anderson et al.*, 1986], are compared to corresponding average irradiance values provided by *Halthore et al.* [2005]. In particular, the irradiance components for the subarctic winter and tropical atmosphere, at two solar zenith angles, 30° and 75°, and for a wavelength-independent Lambertian surface albedo of 0.2, are compared to corresponding average irradiances provided by *Halthore et al.* [2005]. The percentage differences between the irradiance values provided by this model and the corresponding ones given by *Halthore et al.* [2005, Table 2] are lower than 10% and, in general, the agreement is better for the low solar zenith angle (30°), according to *Halthore et al.* [2005] findings. To further support the appropriateness of model input and output data, we provide in section 5 a closure study of modeled and experimental net fluxes at the surface.

2.1. Meteorological Parameters and Atmospheric Molecules

[8] All available 2003 and 2004 radiosonde measurements (see also http://raob.fsl.noaa.gov) at the meteorological station of Brindisi, 40 km northwest of Lecce, have been used to define monthly mean vertical profiles of density, pressure, temperature, and water vapor from 0 up to 20 km altitude. As example the vertical profiles of temperature and water vapor are illustrated in Figures 1 and 2, respectively. Above 20 km of altitude, vertical profiles of density, pressure, temperature, and water vapor are extended with corresponding midlatitudes standard atmosphere data provided by the Air Force Geophysics Laboratory (AFGL) for autumn-winter and spring-summer months.

[9] The Rayleigh scattering due to atmospheric molecules is considered in the model and air molecules are treated as particles with a wavelength (λ) dependent extinction ($\propto \lambda^{-4}$),

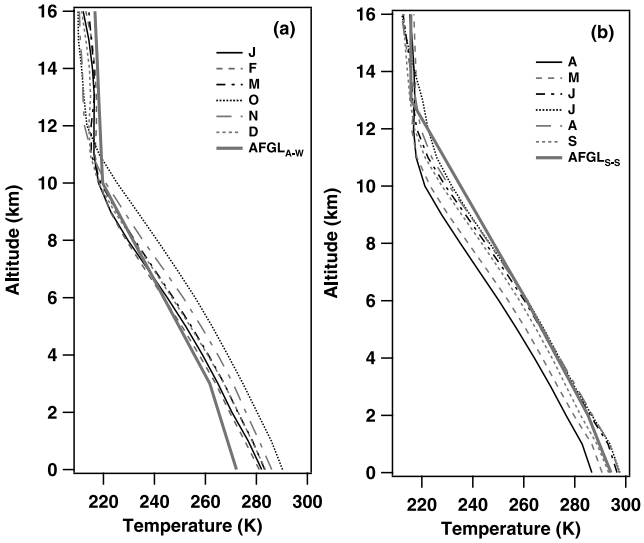

Figure 1. Monthly averaged vertical profiles of the air temperature for (a) autumn-winter months and (b) spring-summer months. Thick shaded lines represent midlatitude vertical profiles of the air temperature provided by AFGL for autumn-winter (Figure 1a) and spring-summer (Figure 1b).

single-scattering albedo equal to one, and asymmetry factor equal to null value.

2.2. Cloud Cover

[10] An appropriate assumption of the spatial and temporal distributions of clouds is necessary to properly estimate aerosol direct radiative effects [e.g., *Takemura et al.*, 2002]. In this paper, we make use of monthly cloud climatologies to better represent clouds typical of the study area. In

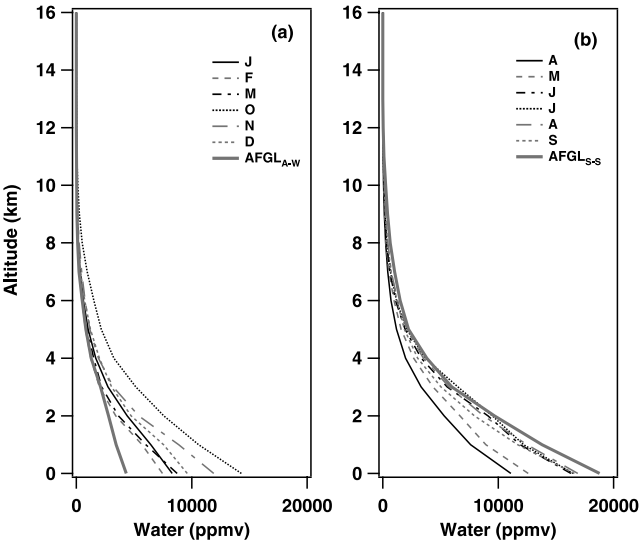

Figure 2. Monthly averaged vertical profiles of water vapor in (a) autumn-winter and (b) spring-summer. The thick shaded line represents the midlatitude water vapor vertical profile provided by AFGL for (a) autumn-winter and (b) spring-summer.

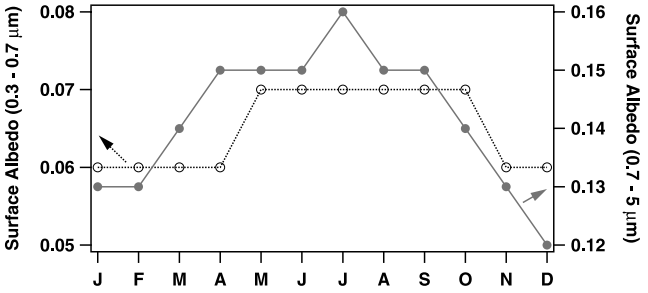

Figure 3. Monthly averaged solar surface albedo based on MODIS products for visible (open dots) and near-infrared (shaded dots) wavelengths.

particular, cloud properties are defined by monthly means of scene optical depth and cover for high-level, midlevel and low-level clouds of multiyear ISCCP D2 data [*Rossow and Schiffer*, 1999]. For the distribution of the optical depth over the three cloud layers, initially assumed optical depths of 2 for cirrus (high), 4 for altostratus (mid), and 10 for cumulus (low) are each scaled by an identical factor, so that the cloud cover combined total cloud optical depth matched the ISCCP's scene optical depth. The altitude location of high-level, midlevel, and low-level clouds is assumed to vary on a monthly basis for high-level and midlevel clouds, according to the ISCCP classification. Microphysical properties of C1, C5 [*Deirmendjian*, 1969], and cirrostratus are assumed for low-level, midlevel and high-level clouds. In particular, single scattering properties typical of ice crystals

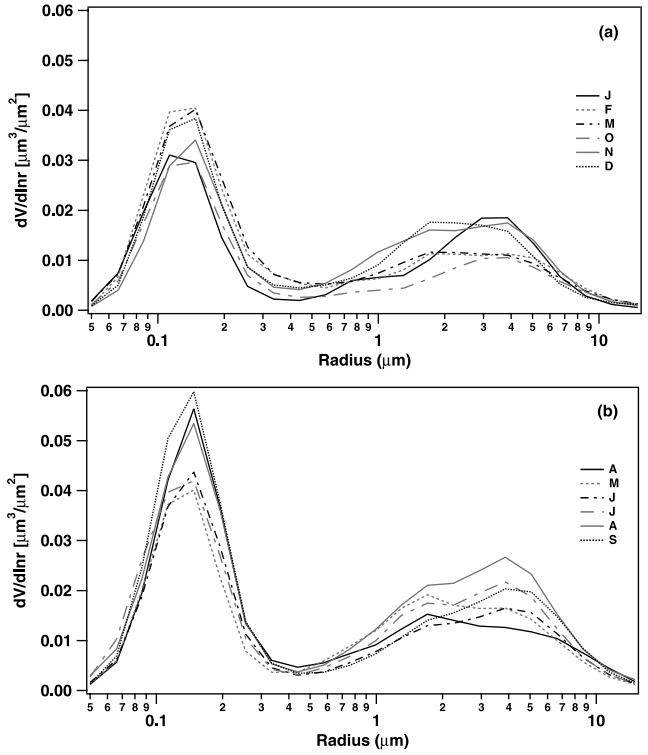

Figure 4. Monthly averaged volume size distributions retrieved by AERONET Sun/sky photometer measurements during (a) autumn-winter and (b) spring-summer months of the 2003–2004 years.

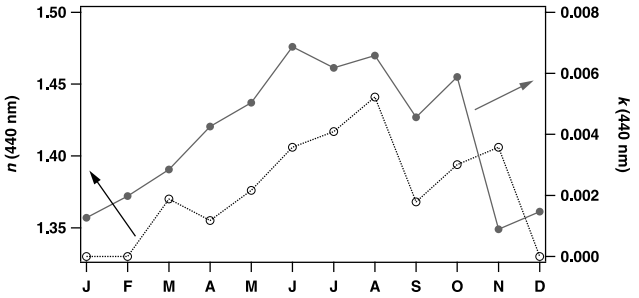

Figure 5. Monthly averaged real (open dots) and imaginary (shaded dots) refractive indices at 440 nm retrieved by Sun photometer measurements.

(e.g., larger sizes and asymmetry factors of about 0.8) are assumed for the high-altitude clouds [*Heymsfield*, 1975]. All-sky (with clouds) radiative transfer simulations assume random cloud overlap among the 3 discrete cloud layers and simulate the aerosol forcing for all 8 different cloud configurations (e.g., no clouds, all 3 clouds, etc. . .) according to the given cloud cover fraction [*Rossow et al.*, 1993].

2.3. Surface Albedo

[11] The used monthly means of the surface albedo are based on MODIS satellite sensor data for the 2003–2004 years. In particular, the filled land surface albedo statistical product from MOD43B3 that is provided at 1° × 1° resolution, is used. Figure 3 shows monthly averaged surface albedo values for visible (open dots) and near-infrared (shaded dots) wavelengths retrieved for the 1° × 1° cell centered at Lecce. The geographical cell covers both land and ocean and land cover of this cell is approximately 25%. The infrared ground emissivity has been set to 99%.

2.4. Aerosol Data

[12] Aerosol size distributions and refractive indices characterize aerosol properties. The relevant data in this paper are based on inversions of CIMEL Sun/sky photometer measurements performed from March 2003 to October 2004 at Lecce (40.33°N, 18.10°E). The CIMEL instrument is operating within AERONET. Figures 4a and 4b show monthly averaged volume size distributions (dV(r)/dlnr) for autumn-winter (from October to March) and spring-summer (from April to September) months, respectively. Analyses by *Dubovik et al.* [2000, 2002] have shown that dV(r)/dlnr values are retrieved with accuracy levels of the order of 15–35% for 0.1 μm $\leq$ r $\leq$ 7 μm. However, the errors in estimating very small values of dV(r)/dlnr (for example, the values on the tails of the size distribution at r < 0.1 μm and r > 0.7 μm) can be much higher. Figure 4 indicates that the volume (and mass) of aerosols smaller than 1 μm in maximum dimension (fine mode) dominate during all year, particularly during spring and summer. However, the bimodal structure of the spectrum indicates that along with fine mode particles, which are mainly of anthropogenic origin, coarse mode particles as those of natural (marine and crustal) origin, also contribute to the aerosol load during all year. Monthly averages for real *n* and imaginary *k* refractive indices at λ = 440 nm are plotted on Figure 5 as an example. According to *Dubovik et al.* [2000, 2002], the expected accuracy for the real part of the refractive index is of 0.04 for AOT (440 nm) $\geq$0.5 and of 0.05 for AOT (440 nm) $\leq$0.2. *k* values are instead retrieved with errors of the order of 30–50% for AOT (440 nm) $\geq$0.5 and of the order of 80–100% for AOT (440 nm) $\leq$0.2. *n* and *k* values that display the largest values during summer and late fall, indicate that pollution dominates AOT contribution during that period.

[13] For the near-infrared region of the solar spectrum, the AERONET refractive indices extracted for the wavelength at 1.02 μm are applied. For the far-infrared spectral region the refractive indices for tropospheric aerosol [*Paltridge and Platt*, 1976] are used. Mie calculations (assuming a spherical particle shape) are performed to translate the data on size, concentration and refractive indices into optical depth (a measure for amount), single scattering albedo (a measure for absorption) and asymmetry factor (capturing the angular scattering behavior). Monthly mean values of aerosol optical thickness (AOT) and single scattering albedo (SSA) at 550 nm are plotted in Figure 6a. Only during spring and summer AOTs exceed 0.15 and SSA values fall below 0.95. It is worth mentioning that in a recent paper [*Santese et al.*, 2007] some of the authors have shown that AERONET AOTs at 550 nm retrieved from 2003–2004 year measurements, were well correlated (correlation coefficient = 0.88) to MODIS AOTs (550 nm) colocated in space and time.

[14] Figure 6b separates fine (open dots) and coarse (shaded dots) mode AOTs, resulting in AOT_{fine}/AOT_{coarse} ratios between 2 and 6. Figures 4–6 reveal that all aerosol parameters display a marked seasonality and that fine mode absorbing particles dominate during spring and summer. A detailed discussion on the seasonal dependence of the aerosol properties retrieved over southeast Italy by Sun/sky photometer measurements is given by *Perrone et al.* [2005]. To better understand the seasonal dependence of the aerosol parameters plotted on Figures 4–6 and hence the seasonal dependence of the aerosol DREs, we remind here

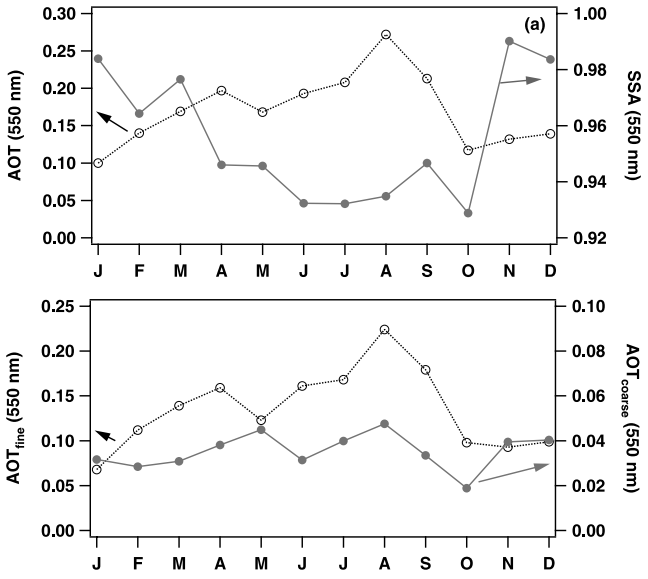

Figure 6. (a) Monthly averaged AOTs (open dots) and SSAs (shaded dots) at 550 nm. (b) Monthly averaged values of AOT_{fine} (open dots) and AOT_{coarse} (shaded dots) at 550 nm.

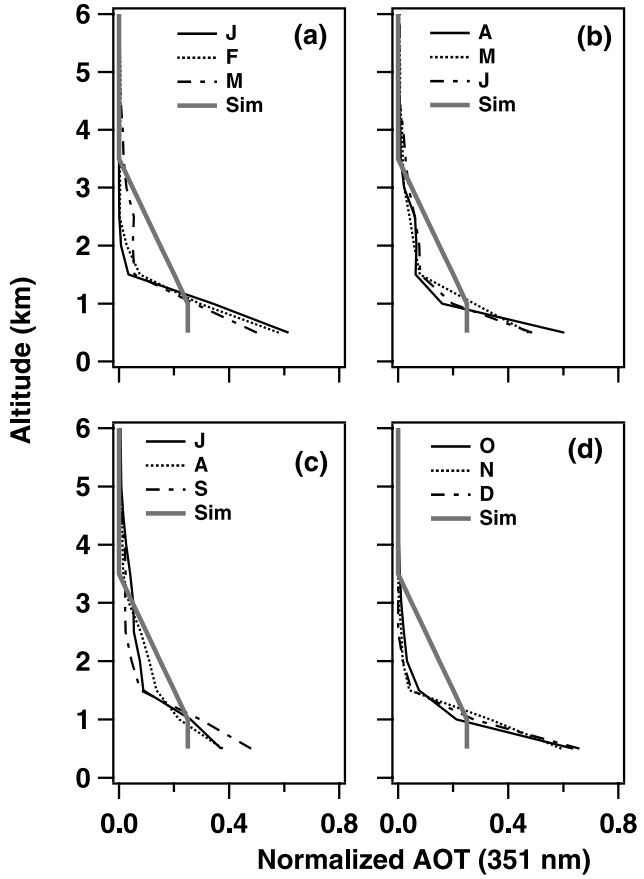

Figure 7. (a–d) Monthly averaged aerosol vertical profiles retrieved by lidar measurements at 351 nm as a function of the normalized AOT and the simulated aerosol vertical profile (thick shaded line).

that the AERONET data of this paper have been retrieved from measurements performed at a southeastern Italy site that is at about 20 km from the Ionic and Adriatic Sea, respectively, in the central-east Mediterranean basin. The Mediterranean Sea is situated to the south of highly populated European countries with industrial, semi-industrial, and rural economies, and to the north of African deserts. Because of the variety of the regions around the basin, different aerosol types can be found in the Mediterranean atmosphere: desert dust from the Sahara desert and the arid regions in the Iberian Peninsula, polluted particles from urban and industrial areas of north and east Europe, marine aerosols from the Mediterranean itself or transported from the Atlantic, and biomass burning particles, often produced in forest fire, mainly during the summer [*Lelieveld et al.*, 2002]. Yearly based back trajectory analyses have revealed that more than 60% of air masses which arrive in the central-east Mediterranean come from N-NW Europe and 13–16% from the Sahara [e.g., *Guerzoni et al.*, 1990; *Smolik et al.*, 2003]. Low-pressure systems in North Africa and in the south Mediterranean drive desert dust to the central-east Mediterranean. Air masses from north and northeast Europe contain particles emitted or derived from industrial and urban sources; while those from Sahara carry predominantly mineral dust. Moreover, the summer time over the Mediterranean is characterized by strong sunlight causing photochemical smog [e.g., *Smolik et al.*, 2003] and by stable atmospheric conditions, which favor the accumulation of aerosol particles. Forest fires, which occur during the summer months in the Mediterranean region and North Africa, also contribute to increase black carbon and fine particle emissions during summer months [e.g., *Pace et al.*, 2006]. Thus the Mediterranean represents an area where aerosols from different natural and anthropogenic sources can be present at all times. Anthropogenic particles mainly account for the fine-mode aerosol fraction, while natural particles account for the coarse-mode fraction. As a consequence, Figure 4 reveals that the aerosol size distribution is bimodal during all year. As we have mentioned, the larger contribution of fine-mode particles (Figures 4b, 5, and 6) and the larger n and k values (Figure 5) observed in summer can partially be ascribed to the stable atmospheric conditions and the strong sunlight that characterize the summer time over the Mediterranean basin and favor both the accumulation of anthropogenic particles and the formation of photochemical smog. In addition to the less stable atmospheric conditions, precipitation scavenging during the rainy season mainly between October and March reduces aerosol concentrations. As consequence, the percentage contribution of marine aerosols from the sea surface may get more significant during autumn-winter months when the contribution of long-range transported aerosols is less significant over the Mediterranean. Marine aerosols represent an important component of the aerosol load of coastal sites like Lecce during all year [*Perrone et al.*, 2005]. We believe that the larger percentage contribution of marine aerosols during winter times may account for the smaller winter values of n and k revealed by Figure 5. In addition, relative humidity that is on average larger in autumn-winter at all altitudes, helps water-soluble and sea-salt particles to become more dominant during winter and may also partially account for the winter refractive index values that are closer to those of water.

[15] The aerosol vertical distribution is based on monthly means of lidar measurements at 351 nm performed during 2003 and 2004 at Lecce (40.33°N, 18.10°E). The lidar monitoring has been performed within the European Project EARLINET. Figures 7a–7d (solid lines) show the monthly evolution of the aerosol vertical profile normalized to the aerosol optical thickness at 351 nm. Descriptions of the lidar system and measurements are given by *De Tomasi and Perrone* [2003], but we remind that the lidar system is based on a XeF excimer laser operating at 351 nm and a Newtonian telescope, whose primary mirror has 30 cm diameter and 120 cm focal length. The lidar system allows getting backscatter coefficient vertical profiles at daytime, while simultaneous measurements of extinction and backscatter coefficient vertical profiles are limited to nighttime. Figures 7a–7d reveal that the averaged maximum height at which aerosol are detected by the lidar is about 5 km during spring and summer, but only near 3 km during autumn and winter. The scarce renovation of air masses, occurring in spring-summer as a consequence of the stable atmospheric conditions, favors the accumulation of the atmospheric aerosol particles and may account for the larger aerosol optical depths (Figure 6a, open dots) and the higher altitudes at which aerosol are detected by the lidar [*De*

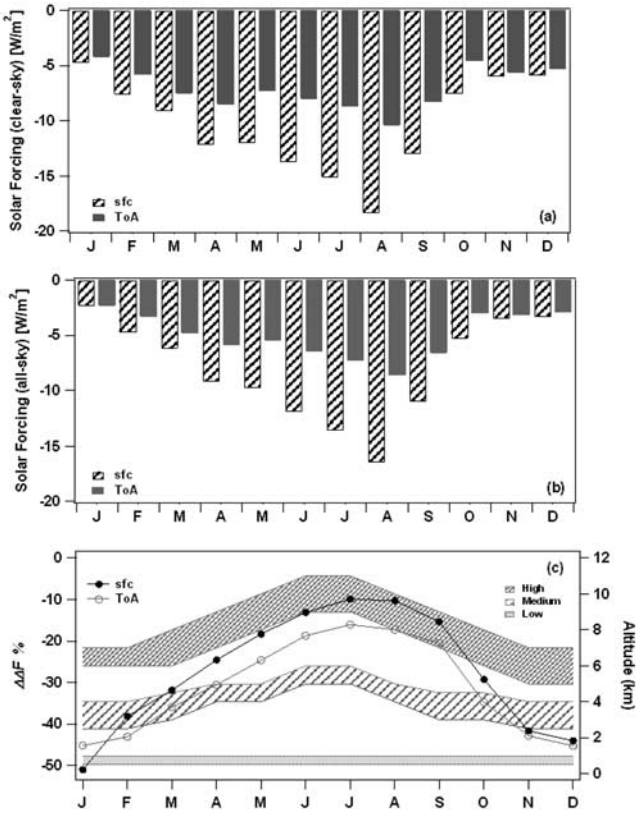

Figure 8. Monthly evolution of the solar (0.3–3.5 μm) aerosol DRE at the ToA (shaded bars) and at the surface (dashed bars) under (a) clear-sky and (b) all-sky conditions. (c) Percentage differences between all-sky and clear-sky conditions of the solar (0.3–3.5 μm) aerosol DRE, at the ToA (open dots) and at the surface (solid dots). Dashed areas represent the altitude location of low-, medium-, and high-level clouds.

Tomasi et al., 2006]. According to *De Tomasi et al.* [2006], monthly averaged lidar profiles are not significantly affected by dust events from African deserts: the differences between the profiles retrieved by taking into account the data points retrieved during dusty days and those obtained by taking away the dusty days data points are lower than corresponding standard errors at all altitudes. Transport of Saharan dust occurs mostly during the spring and summer and causes sporadic crustal aerosol pulses to the Mediterranean area [e.g., *Bergametti et al.*, 1989; *De Tomasi et al.*, 2003].

3. Methodology and Results

[16] A common way to quantify impacts of atmospheric changes to the Earth-atmosphere system is the determination of the associated change to the radiative energy balance. In so-called radiative forcing simulations, changes in radiative (net) fluxes due to modifications of the parameter of interest are computed by means of two simulations. Of particular interest are changes at the Top of Atmosphere (ToA) and at the surface (sfc). ToA forcing summarizes the impact to the entire Earth-atmosphere system, and surface forcing captures the impact on exchange processes between atmosphere and the Earth's surface. Here, the focus is on the mean annual impact of aerosols over southeastern Italy.

[17] Monthly aerosol DRE simulations are based on the 2003–2004 input data listed above. We point out that calculated aerosol direct radiative effects are not simply based on monthly averaged aerosol properties. To account for the aerosol property variability within a month, we consider in the paper that microphysical and optical aerosol properties are linked to AOT changes. So, all size distribution and refractive index values retrieved by AERONET measurements performed within a month are divided into five equal number bins according to the AOT strength. Bin mean values of size distributions and refractive indices are used to calculate aerosol DREs of each bin. Then, the output data provided by the five separate simulations, one for each bin data set, are summed to get monthly values of the aerosol DRE. We believe that this procedure allows addressing the variability of aerosol properties within a month.

[18] The radiative forcing calculated here does not include (time-evolving) indirect aerosol effects on properties of atmosphere (e.g., clouds, precipitation) or surface (e.g., vegetation, albedo). The simulations only address the instantaneous impact due to the presence of all (natural and anthropogenic) aerosols, the aerosol direct radiative effect (DRE). Results based on 2003–2004 monthly averaged data, are summarized in Figures 8–12. Aerosol direct radiative effects are separately discussed for solar and infrared spectral regions. An aerosol DRE is considered negative at the ToA, if more energy is lost to the Earth-atmosphere system (e.g., increased solar reflection or plan-

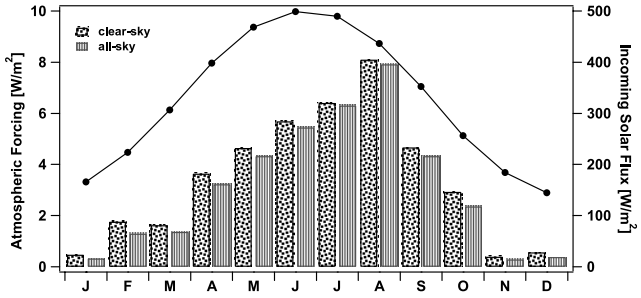

Figure 9. Monthly averaged atmospheric forcing (left axis) under clear-sky (dotted bars) and all-sky (dashed bars) conditions, and monthly averaged values of the incoming solar flux (solid dots).

etary cooling) and at the surface, if less energy reaches the ground (e.g., solar dimming or surface cooling).

3.1. Results on ToA and Surface Aerosol Direct Radiative Effect at Solar Wavelengths (0.3–3.5 μm)

[19] ToA monthly values of the aerosol DRE, at solar wavelengths, are plotted in Figures 8a and 8b (shaded bars) for clear- and all-sky conditions, respectively. Figure 8c shows the altitude location of high-level, midlevel, and low-level clouds. The corresponding solar aerosol DRE at the surface is given in Figures 8a and 8b (dashed bars). Monthly averaged ToA aerosol DREs are negative throughout the year. This demonstrates a cooling of the Earth-atmosphere system by aerosols, as mainly extra solar radiation is reflected back to space. Aerosol associated reductions of the downward solar radiation at the Earth's surface are larger, as aerosols not only scatter but also absorb solar radiation: larger aerosol solar absorptions determine larger differences

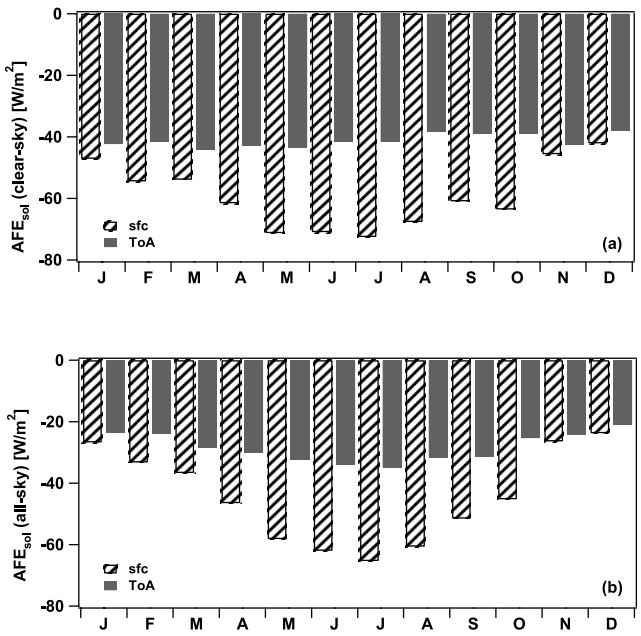

Figure 10. Monthly averaged values of the solar (0.3–3.5 μm) aerosol DRE efficiencies at the ToA (shaded bars) and at the surface (dashed bars) under (a) clear-sky and (b) all-sky conditions.

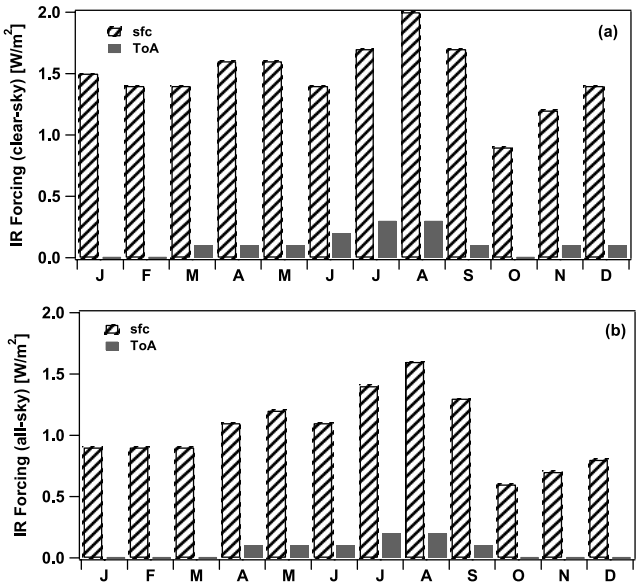

Figure 11. Monthly evolution of the infrared (4–80 μm) aerosol DRE at the ToA (shaded bars) and at the surface (dashed bars) under (a) clear-sky and (b) all-sky conditions.

between ToA and surface aerosol DREs. At Lecce surface aerosol DREs are in summer about twice aerosol DREs at the ToA. We point out that incoming solar flux values also are, in summer, twice the winter values (Figure 9, solid dots). Similar results have been reported by several authors [*Hatzianastassiou et al.*, 2004; *Kaufman et al.*, 2002; *Ramanathan et al.*, 2001]. In particular, aerosol DRE calculations based on measurements performed in summer

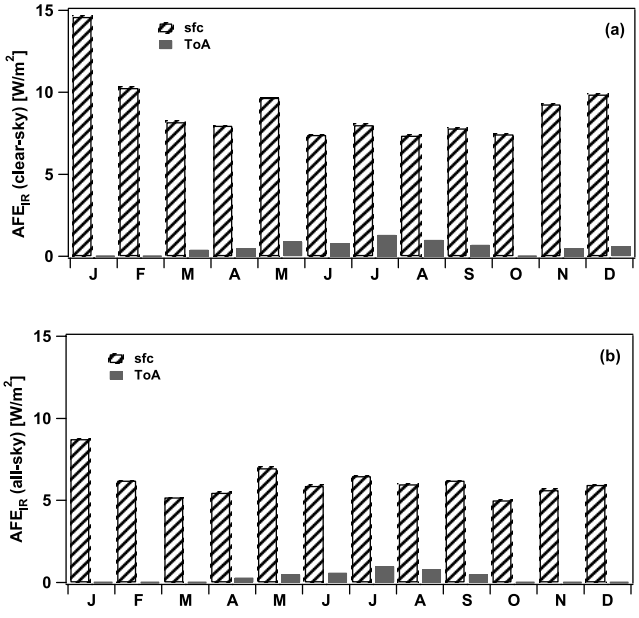

Figure 12. Monthly averaged values of the infrared (4–80 μm) aerosol forcing efficiency at the ToA (shaded bars) and at the surface (dashed bars) under (a) clear-sky and (b) all-sky conditions, which are defined as the aerosol DRE per unit of AOT at 550 nm.

2001 at Crete (Greece) during the Mediterranean Intensive Oxidation Study, have revealed that aerosols can produce locally at the surface an effect 2.7 times larger than their effect at the ToA [*Lelieveld et al.*, 2002].

[20] Figure 8 reveals a marked seasonal evolution of the aerosol DRE at the ToA and at the surface both under clear-sky (Figure 8a) and all-sky (Figure 8b) conditions. Figure 8 shows that the solar aerosol DRE for clear-sky conditions (Figure 8a, shaded bars) ranges at the ToA from -4.2 W/m^2 in January to -10.4 W/m^2 in August and at the surface from -4.7 W/m^2 in January to -18.4 W/m^2 in August. The summer values at the surface are consistent with (daily) DRE values derived from measurements of a summer campaign in Crete [*Lelieveld et al.*, 2002]. The seasonal cycle of available solar radiation (see Figure 9, solid dots) is primarily responsible for the seasonal variability of the aerosol DRE. The seasonal changes of the aerosol properties are a contributing factor and are mainly responsible for the asymmetric trend of the aerosol DRE seasonal variability. Aerosol loads (Figure 6a, open dots) and maximum aerosol heights (Figure 7) display maxima in summer and minima in winter [e.g., *De Tomasi et al.*, 2006]. During summer, contributions of small absorbing aerosol particles are largest, as both properties, the AOT_{fine}/AOT_{coarse} ratio (Figure 6b) and the real and imaginary part of the refractive index (Figure 5), display summer maxima [e.g., *Perrone et al.*, 2005]. In accordance to the discussion of section 2.4, a major explanation is the scarce renovation of air masses during Mediterranean summers, as a consequence of the weather stability [*Perrone et al.*, 2005]. Asides forest fires, which occur during the summer months in the Mediterranean region and North Africa and increase black carbon and fine particle emissions [e.g., *Pace et al.*, 2006], the more abundant solar flux in summer is likely to enhance the production of secondary aerosols [*Seinfeld and Pandis*, 1998].

[21] At all-sky conditions, the solar aerosol DRE reduces in magnitude, since clouds reflect solar radiation back to space and reduce sunlight available for aerosol interactions. The comparison of Figures 7 and 8c reveals that aerosols are placed within low-level and midlevel clouds and are always located below high-level clouds. The presence of aerosols above clouds, which can dim cloud brightness to space, may be an additional reason for a less negative ToA aerosol DRE under all-sky conditions. The percentage reduction with respect to the clear-sky aerosol DRE (Figure 8c, ToA: open dots, surface: solid dots) is larger in winter (approximately -45%) than in summer (approximately -20%) in part because there is less cloud cover during summer.

[22] The atmospheric forcing (AF) is defined as the difference between the solar ToA and the solar surface aerosol DRE. It represents the solar radiative flux that is stored in the atmosphere to heat the aerosol layer. Vertical profiles of Figures 7a–7d place such aerosol solar heating in the lower 5 km during spring-summer and in the lower 3 km during autumn-winter. The AF is an indicator of the aerosol effects on the atmospheric dynamics. The aerosol warming in the lower troposphere can slow the hydrological cycle, reduce evaporation from the surface and reduce cloud formation [*Kaufman et al.*, 2002]. Column averaged clear-sky AF is usually less than 1 W/m^2 during winter, but can reach values near 8 W/m^2 in summer (Figure 9, dotted and dashed bars). All-sky AF (Figure 9, shaded bars) is similar to clear-sky AF, as in presence of clouds two counteracting effects largely cancel each other: (1) absorbing aerosol above clouds enhances aerosol absorption and (2) less solar radiation for aerosol below clouds reduces aerosol absorption. The AF seasonality is well correlated with annual cycles of available sunlight and aerosol amount. The maximum shift into late summer is attributed to the maximum aerosol loads partially because of the lack of air mass exchange during the warm dry season. For comparison, mean monthly values of the incoming solar flux F_o are plotted in Figure 9 (solid dots): F_o follows the annual cycle of the daytime hours and hence reaches its maximum value on June.

[23] Aerosol DRE calculations over the Mediterranean by *Lelieveld et al.* [2002] suggest an atmospheric forcing of more than 11 W/m^2 on summer, as consequence of the solar radiation absorption by black carbon, and possibly by dust, fly ash or organic carbon, much of which is in the lower 4 km. According to *Lelieveld et al.* [2002], the large reduction in surface solar radiation by aerosol, occurring on summer over the Mediterranean, is similar to that observed over the northern Indian Ocean in Asian pollution outflow [*Ramanathan et al.*, 2001].

[24] If only data on aerosol optical thickness are available, such as from satellite retrievals, then it is often desirable to know the local aerosol forcing efficiency AFE (aerosol DRE per unit optical depth) to translate an AOT value into its associate aerosol DRE: aerosol forcing efficiencies are mainly dependent on aerosol size and composition. Here, calculated AFE refers to the aerosol optical depth at 550 nm. Clear-sky AFEs at ToA (shaded bars in Figure 10a) are almost constant during the entire year at a value of about -40 W/m^2. This is the result of competing effects by SSA and AOT, as both influence the aerosol DRE at the ToA [*Satheesh*, 2002; *Meloni et al.*, 2005]. The ToA aerosol DRE increases with larger SSA and larger AOT values and Figure 6a shows that the SSA annual cycle is anticorrelated to the AOT annual cycle: on autumn-winter AOTs take smaller values while SSAs assume larger values and the opposite occurs on spring-summer. Hence the larger aerosol absorption (less negative ToA aerosol DRE) combines with the larger scattering due to smaller size (Figure 6b) particles (more negative solar ToA DRE) to produce a balanced effect. This is also consistent with AFE values at the surface, as both larger absorption and smaller size particles combine to more negative AFEs, leading to a summer maximum of about -70 W/m^2 compared to near -45 W/m^2 in winter. In fact, high AOTs and small SSA values decrease the downward solar radiation at the Earth's surface and as a consequence Figure 10 (dashed bars) reveals that AFEs are larger on spring-summer. The forcing efficiency dependence on Sun elevation [e.g., *Russell et al.*, 1999] may represent a contributing factor to the surface AFE annual cycle. In contrast, under all-sky conditions summer maxima are found for forcing efficiencies both at the surface and TOA, since the minimum cloud cover during summer becomes a contributing factor.

3.2. Results on the ToA and Surface Aerosol DRE at Infrared Wavelengths (4–80 μm)

[25] In this section we analyze the longwave (IR) radiation (4–80 μm) aerosol DREs at the surface and at the ToA. The IR effect of tropospheric aerosols is often neglected,

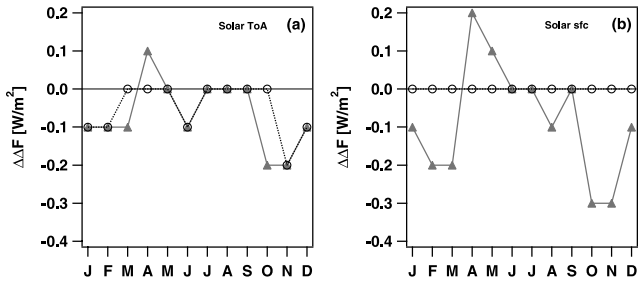

Figure 13. Monthly differences between the solar (0.3–3.5 μm) aerosol DRE calculated by using the AFGL meteorological profiles (shaded triangles) and that of the reference case (a) at the ToA and (b) at the surface under clear-sky conditions. Open dots represent the monthly difference between the solar aerosol DRE calculated by using the simplified aerosol vertical profile and that of the reference case at the ToA (Figure 13a) and at the surface (Figure 13b) under clear-sky conditions.

because the IR forcing is small compared to the solar effect, especially at the ToA. The IR aerosol forcing is usually positive both at the ToA and surface. The IR ToA forcing (also often referred to as greenhouse effect, as thermal energy is retained in the Earth-atmosphere system) requires both significant IR aerosol optical depth (e.g., coarse size aerosols) and a significantly lower temperature compared to that of the thermal energy emitting medium (ground or cloud) below aerosols. Thus a significant IR ToA effect by tropospheric aerosols is only expected from elevated dust layers over cloud-free scenes and warm surfaces. The IR surface forcing requires IR opacity (e.g., coarse size aerosol) at temperatures not too much below that of the surface. Thus largest IR surface effects are expected from coarse (sea salt and dust) aerosols near the surface. A significant effect is also expected in Polar Regions, where warmer aerosols can significantly increase the downward IR radiation at very cold surfaces underneath.

[26] Clear- and all-sky monthly values of the IR aerosol DRE at the ToA are plotted on Figures 11a and 11b (shaded

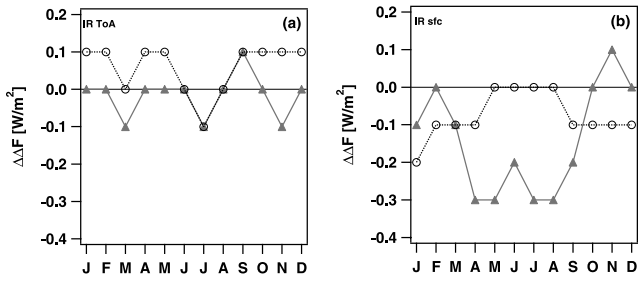

Figure 14. Monthly differences between the infrared (4–80 μm) aerosol DRE calculated by using the AFGL meteorological profiles (shaded triangles) and that of the reference case (a) at the ToA and (b) at the surface under clear-sky conditions. Open dots represent the monthly difference between the infrared aerosol DRE calculated by using the simplified aerosol vertical profile and that of the reference case at the ToA (Figure 14a) and at the surface (Figure 14b) under clear-sky conditions.

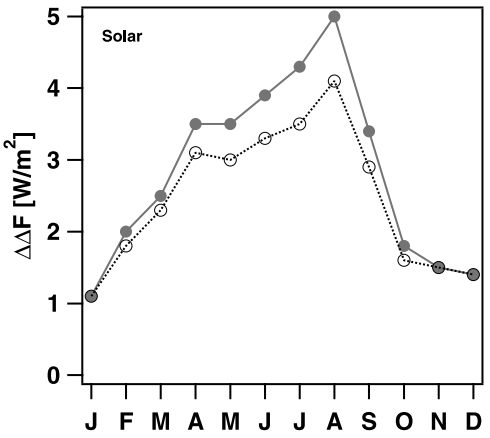

Figure 15. Monthly differences between the solar (0.3–3.5 μm) aerosol DRE calculated using the surface albedo of a barren and sparsely vegetated area and that of the reference case at the ToA (shaded dots) and at the surface (open dots) under clear-sky conditions.

bars), respectively. Corresponding infrared aerosol DREs at the surface are plotted on Figures 11a and 11b (dashed bars). As expected from the aerosol size characteristics, the infrared aerosol DRE is significantly smaller in magnitude compared to the solar aerosol DRE and always positive, being thus opposite in sign to the solar DRE: aerosols produce planetary and surface warming through interaction with IR radiation. At clear-sky conditions the infrared aerosol DRE at the ToA is close to null values during winter and varies within the 0.1–0.3 W/m^2 range during spring-summer. The IR aerosol DRE at the surface varies within the 0.9–2 W/m^2 range without a clear annual cycle, offsetting 10–30% of the (negative) solar aerosol DRE. Figure 11b shows that clouds, because of their own greenhouse effect, reduce the IR aerosol DRE both at the ToA and at the surface. Percentage reductions with respect to the clear-sky IR aerosol DREs are of about 30–40%.

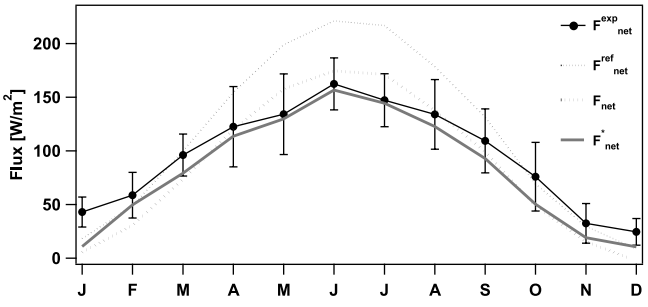

Figure 16. Monthly mean values of the net flux at the surface as experimentally measured (F_{net}^{exp}, solid dots). Error bars represent standard deviations. F_{net}^{ref} (black dotted line) and F_{net} (grey dotted line) represent monthly mean values of the all-sky net flux provided by the model using the MODIS and the barren and sparsely vegetated area surface albedo, respectively. F_{net}^{*} (grey solid line) represents monthly mean values of the all-sky net flux provided by the model for the barren and sparsely vegetated area surface albedo and the Lecce's monthly mean ground temperature values.

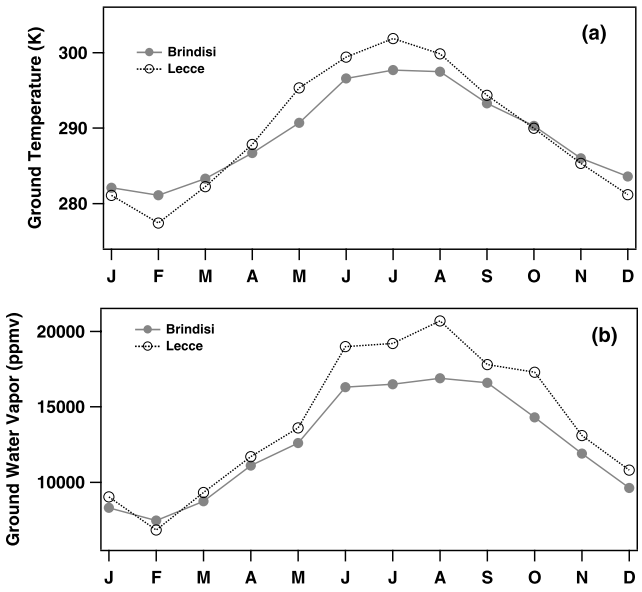

Figure 17. Monthly mean ground values of (a) temperature and (b) water vapor retrieved at Brindisi by radiosounding (shaded dots) and at Lecce (open dots) by ground measurements.

[27] The infrared AFE, defined as the aerosol DRE per unit of aerosol optical depth at 550 nm, is shown on Figures 12a and 12b for clear- and all-sky conditions, respectively. The clear-sky IR AFE at the surface (Figure 12a, dashed bars) displays an annual cycle with slightly larger values on winter. Hence the same unit of AOT produces larger surface AFEs in winter than in summer. AFEs are larger in winter since the aerosol absorption is likely smaller, being relative humidities and wet aerosols larger in winter. The larger percentage of coarse mode particles (such as sea-salt particles) in winter (Figure 6b) may also represent a contributing factor. It may also occur that the increase in temperature due to aerosol absorption, compared to that in absence of aerosols, is larger in winter (low temperatures) than in summer when the air temperature is quite high because of other reasons such as surface heating.

4. Sensitivity Studies

[28] The role of selected aerosol and environmental properties on the aerosol DRE is now investigated. Results of the sensitivity tests are given in terms of absolute and percentage changes of the aerosol DRE, $\Delta\Delta F$ and $\Delta\Delta F\%$ respectively, where:

$$\Delta\Delta F = \Delta F - \Delta F_{ref} \tag{1}$$

$$\Delta\Delta F\% = \left(\frac{\Delta F - \Delta F_{ref}}{\Delta F_{ref}}\right) \cdot 100 \tag{2}$$

[29] ΔF_{ref}, is the aerosol DRE of the reference case and ΔF represents the aerosol DRE obtained after varying a particular property. All sensitivities refer to clear-sky conditions.

4.1. Aerosol Direct Radiative Effect Sensitivity to Clear-Sky Vertical Profiles of Meteorological Parameters

[30] In order to investigate the importance of meteorological parameters profiles (density, pressure, temperature and water vapor content) on the aerosol DRE, we replaced the Brindisi radiosonde data with the AFGL midlatitude (30–60°N) summer profile from April to September and with the AFGL midlatitude winter profiles from October to March (see Figures 1 and 2, shaded lines). Notable differences in the lower troposphere are lower AFGL temperatures and lower AFGL water vapor content in winter, yet larger AFGL temperatures and larger AFGL water vapor content in summer. AFGL relative humidity profiles are, on average, characterized by larger values than radiosonde profiles and, as a consequence, affect trace gas absorption calculations. Aerosol DRE changes due to the switch to AFGL meteorological profiles have only a small impact. Changes to the solar aerosol DRE at the surface and the ToA do not exceed 5% of the reference case (with radiosonde data) as shown in Figures 13a and 13b (shaded triangles).

[31] Changes to the infrared aerosol DREs, as illustrated in Figures 14a and 14b (shaded triangles), that are close to null values at the ToA, are of the order of 20% at the surface. This is still negligible, because the overall infrared impact is small compared to the solar impact. However, it is worth noting from Figure 14b (shaded triangles) that the use of AGFL midlatitude profiles decreases the IR aerosol DRE at the surface on spring-summer. Figure 2b shows that, in the lower troposphere, the spring-summer AGFL midlatitude water vapor profile is characterized by values that are larger than corresponding radiosonde data, and *Markowicz et al.* [2003] have shown that the increase of the column water vapor leads to a larger decrease in the surface aerosol DRE than that at the ToA, in accordance to model results of this paper (Figure 14, shaded triangles).

4.2. Aerosol Direct Radiative Effect Sensitivity to Aerosol Vertical Profiles

[32] To investigate the importance of aerosol vertical distributions on aerosol DRE calculations, we have replaced lidar based (EARLINET) aerosol profile statistics by a simulated profile (shaded line on the plots of Figures 7a–7d), which is representative of a well-mixed aerosol layer extending up to 3 km. Therefore more aerosol optical depth is placed at higher altitudes (and less in altitudes <1 km), mainly during winter, when the simulated profile is used.

[33] Aerosol DRE changes at the surface are negligible and at the ToA are smaller than 4%, as shown in Figures 13b and 13a (open dots), respectively. Latter results are in accordance with those reported in other studies [e.g., *Torres et al.*, 1998; *Meloni et al.*, 2005]. It is worth noting from Figure 13a (open dots) that the simulated profile is more efficient in increasing the radiation scattered back to space on winter months, i.e., when the AOT is placed up to higher altitudes.

[34] Infrared aerosol DRE changes, due to the higher altitude placement of aerosols, reveal the expected increase of the ToA aerosol DRE (Figure 14a, open dots) and the decrease of the surface aerosol DRE (Figure 14b). Nevertheless, IR changes are small in an absolute sense, given the overall magnitude of the infrared aerosol DRE for Lecce.

4.3. Aerosol Direct Radiative Effect Sensitivity to the Surface Albedo

[35] The role of the solar surface albedo on the aerosol DRE is investigated by replacing the MODIS albedo regional averages of about 0.05 (0.3–0.7 μm) and 0.15 (0.7–5 μm) with the surface albedo values of 0.18 (0.3–0.7 μm) and 0.36 (0.7–5 μm). According to *Zhou et al.* [2003], latter values represent the surface albedo of barren and sparsely vegetated areas and do not vary with the time of the year at midlatitudes. We believe that the higher solar surface albedos are more typical for vegetation and dry terrains near Lecce. Note that the $1^\circ \times 1^\circ$ spatial MODIS regional average is largely dominated by the low solar albedo of the surrounding Mediterranean Sea [*Santese et al.*, 2007], being Lecce 20 km away from the Adriatic and Ionian Sea, respectively.

[36] The switch to larger soil albedo values decreases in absolute value the solar aerosol DRE at the TOA and at the surface, as illustrated in Figure 15, because higher surface albedo values decrease the aerosol's potential to change the upwelling radiation and thus net fluxes. Moreover, increasing surface albedo enhances multiple scattering minimizing thus the decrease in downward and absorbed solar radiation at the surface. A similar sensitivity to surface albedo was also reported by *Hatzianastassiou et al.* [2004]. In particular, the more realistic local surface albedo decreases the ToA aerosol DRE by about 50% and the surface aerosol DRE by about 25%. The aerosol DRE differences of Figure 15 can be considered as the differences between the aerosol DRE over the flat Salento peninsula of Italy and that of the surrounding Mediterranean Sea, since at least AOTs of AERONET at Lecce are in overall accordance with colocated regional AOT retrievals of MODIS [*Santese et al.*, 2007].

5. Closure Study of Model and Experimental Net Fluxes at the Surface

[37] Simulated surface net broadband fluxes are compared in this section to broadband net flux measurements at the surface to support the appropriateness of model input and output data. A net radiation transducer with two hemispheric (up and down) sensors (p056 RADNT, by SIAP+MICROS S.r.l., Italy) close to the lidar site, has monitored broadband (0.3–30 μm) net fluxes in the 2003–2004 years. Daily mean values of the ground net flux have then been used to calculate the monthly mean values F_{net}^{exp} and corresponding standard deviations (dots and error bars) plotted in Figure 16. Corresponding simulated surface net fluxes are provided in Figure 16 in conjunction with MODIS (F_{net}^{ref}) (black dotted line) and with barren vegetated (F_{net}) (grey dotted line) solar surface albedos. According to the discussion of section 4.3, the barren vegetated solar surface is more typical to Lecce. Comparisons to the measured net fluxes show that the agreement with the use of higher surface albedo data is much improved and is within the measurement error bars, except for winter. We have also observed that the winter disagreement could be largely removed by replacing the radiosounding surface temperatures retrieved at Brindisi with surface temperatures more appropriate for Lecce. Figure 17 shows ground monthly mean values of temperature and water vapor retrieved by a ground meteorological station at Lecce and by radio soundings at Brindisi. We observe from Figure 17 that ground temperatures at Lecce and at Brindisi can be by up to 5 K different. Brindisi is on the sea, while Lecce is at about 20 km from the sea shore and, as a consequence, Brindisi's ground temperatures are warmer in winter and colder in summer than Lecce's temperatures. It is worth mentioning that the differences between Lecce and Brindisi meteorological parameter values generally reduce with altitude. The net flux at the surface calculated by using surface temperatures more appropriate for Lecce is plotted on Figure 16 by a solid grey line (F'_{net}). The use of Lecce ground temperatures decreases net fluxes up to 18% in summer and increases net fluxes up to $\sim$5 times during winter. We have also observed that when Lecce water vapor values (Figure 17, open dots) are used in the model, ground net fluxes increase less than 3% on spring-summer and up to 10% on autumn-winter. In summary, Figure 16 reveals that simulated and experimental net flux values (grey and black solid line, respectively) are in good accordance, especially during spring and summer when Lecce appropriate ground temperatures are used. Recent sensitivity studies by *Pavlakis et al.* [2004], on downwelling longwave fluxes at the surface, have also revealed that their model was able to reproduce the observed downwelling longwave flux at a specific station very well, by using local meteorological data. In particular, they have found that the downwelling longwave flux can increase in some regions by up to 11 W/m^2 for a 2 K temperature, in accordance with the results of this paper.

[38] The differences between F'_{net} and corresponding experimental values (Figure 15) that are larger on autumn-winter months may be due either to a poor parameterization of clouds on autumn-winter months and to the larger uncertainties of AERONET products retrieved at low AOT (440 nm) $\leq$0.2. The spectral range (0.3–30 μm) of the net radiation transducer that is smaller than the spectral range (0.3–80 μm) of the model simulations may represent a contributing factor.

[39] Finally, it is worth mentioning that, even if Lecce appropriate ground temperatures have a large impact on surface net fluxes, they affect the total (solar + infrared) aerosol radiative forcing less than 0.3% and 2.6% at the surface and ToA, respectively, in accordance to the results of section 4.1.

6. Summary and Conclusion

[40] The paper reports on the annual cycle of the aerosol DRE over southeast Italy, which possibly can be considered as representative for the central-east Mediterranean. Radiative transfer computations are performed using meteorological data from radiosondes, EARLINET lidar data for aerosol vertical distributions, AERONET Sun/sky photometer data for aerosol microphysical properties, and MODIS surface albedos all referring to 2003–2004 years. The monthly solar and infrared aerosol DRE is calculated at the top of the atmosphere, within the atmosphere and at the Earth's surface, for clear-sky and all-sky conditions. It is shown that, compared to solar aerosol DRE, the IR aerosol DRE is significantly smaller in magnitude and positive. The clear- and all-sky IR aerosol DRE varies at the ToA, within

the 0.1–0.3 W/m^2 range. At the surface, it varies within the 0.9–2 W/m^2 range without a clear annual cycle. On the contrary, the solar aerosol DRE has a strong seasonality, mainly due to the available sunlight, but also influenced by variations in aerosol properties (e.g., composition, size, and amount). Under clear-sky conditions, the winter aerosol DRE varies within $-(6 \pm 2)$ W/m^2 at the ToA and $-(7 \pm 2)$ W/m^2 at the surface, while the summer aerosol DRE varies within $-(9 \pm 1)$ W/m^2 at the ToA and $-(15 \pm 3)$ W/m^2 at the surface. Hence aerosols produce a cooling effect both at the TOA and at the Earth's surface and maximum aerosol DRE values appear in late summer. In addition, a significant heating of the aerosol layer (atmospheric forcing) with late summer values (up to $\sim$8 W/m^2) comparable to the ToA aerosol DRE is observed. According to the comments of section 2.4, these last results can be due either to strong sunlight of summer time that causes photochemical smog and to the scarce renovation of air masses, occurring on summer over all the Mediterranean, as a consequence of the weather stability, which favors the accumulation of local and long-range transported fine mode particles mainly of anthropogenic origin. Forest fires, which occur during the summer months in the Mediterranean region and North Africa, also contribute to the increased black carbon and fine particle emissions in summer.

[41] Under all-sky conditions, the solar aerosol DRE decreases in winter by about 45% both at the surface and at the ToA. On the contrary, it decreases by about 10% at the surface and by $\sim$20% at the ToA, on summer.

[42] In the context of warming by anthropogenic greenhouse gases, only the anthropogenic aerosol fraction under realistic all-sky conditions must be considered. Hence, as example, by assuming that the anthropogenic aerosol fraction decreases the all-sky ToA aerosol DRE by about 40%, still $\sim$60% of the modeled all-sky ToA forcing over southeast Italy is sufficient, except during winter, to compensate the anthropogenic greenhouse warming, which is of $\sim$2.5 W/m^2, according to the World Meteorological Organization (http://www.wmo.ch/web/arep/gaw/gaw_home.html).

[43] In sensitivity studies the relatively weak impact of local meteorological parameters and aerosol vertical profiles with respect to climatological profiles, and the strong impact of the surface albedo is demonstrated. Locally at Lecce the soil albedo is much higher than the albedo applied in the reference case study, which is more characteristic of the ocean surface surrounding the Salento peninsula on which Lecce is located. Thus it is shown that at Lecce and over the land surfaces near Lecce, the more realistic local surface albedo decreases the ToA aerosol DRE by about 50% and the surface aerosol DRE by about 25%.

[44] Observed and model net fluxes at the surface are also compared in a closure study to better support input and output model data. It is shown that the differences between modeled and measured net fluxes are within the expected measurement uncertainty, especially during spring and summer.

[45] Most available studies on the aerosol direct radiative effects over the Mediterranean refer to dedicated campaigns during special pollution events (e.g., Sahara dust outbreaks) and mainly account for the solar aerosol DRE. Here, in contrast, the complete annual cycle of the aerosol impact on the solar and IR aerosol direct radiative effect under clear- and all-sky conditions has been presented. Correlation studies [*Santese et al.*, 2007] have indicated that local samples for aerosol properties (AOTs and fine fraction parameters) closely match regional averages retrieved by satellite (e.g., MODIS). Thus it is possible to extend the findings of this work to larger spatial scales, e.g., to the surrounding region, in conjunction with the proper solar surface albedo.

[46] **Acknowledgments.** This work has been supported by Ministero dell' Istruzione dell'Università e della Ricerca of Italy, (Programma di Ricerca 2004, Prot. 2004023854) and by the European Project EARLINET-ASOS (2006–2010, contract 025991). Authors thank P. Martano of ISAC-CNR for the fruitful discussions on radiative net fluxes and for providing us the data of the net radiation transducer measurements. Reviewers are kindly acknowledged since their comments have significantly contributed to improve the paper.

References

Anderson, G. P., S. A. Clough, F. X. Kneizys, J. H. Chetwynd, and E. P. Shettle (1986), AFGL atmospheric constituent profiles (0–120 km), *Rep. AFGL-TR-86-0110*, Air Force Geophys. Lab., Hanscom Air Force Base, Mass.

Andreae, T. W., M. O. Andreae, C. Ichoku, W. Maenhaut, J. Cafmeyer, A. Karnieli, and L. Orlovsky (2002), Light scattering by dust and anthropogenic aerosol at a remote site in the Negev desert, Israel, *J. Geophys. Res.*, *107*(D2), 4008, doi:10.1029/2001JD900252.

Bergametti, G., L. Dutot, P. Buat-Menard, and E. Remoudaki (1989), Seasonal variability of the elemental composition of atmospheric aerosol particles over the northwestern Mediterranean, *Tellus, Ser. B*, *41*, 553–561.

Bösenberg, J., et al. (2003), A European aerosol research lidar network to establish an aerosol climatology, *MPI-Rep. 348*, Max-Planck-Inst. für Meteorol., Hamburg, Germany.

Boucher, O. (1998), On aerosol direct shortwave forcing and the Henyey-Greenstein phase function, *J. Atmos. Sci.*, *55*, 128–134.

Deirmendjian, D. (1969), *Electromagnetic Scattering on Spherical Polydispersions*, 290 pp., Elsevier, New York.

De Tomasi, F., and M. R. Perrone (2003), Lidar measurements of tropospheric water vapor and aerosol profiles over southeastern Italy, *J. Geophys. Res.*, *108*(D9), 4286, doi:10.1029/2002JD002781.

De Tomasi, F., A. Blanco, and M. R. Perrone (2003), Raman lidar monitoring of extinction and backscattering of Africa dust layers and dust characterization, *Appl. Opt.*, *42*, 1699–1709.

De Tomasi, F., A. M. Tafuro, and M. R. Perrone (2006), Height and seasonal dependence of aerosol optical properties over southeast Italy, *J. Geophys. Res.*, *111*, D10203, doi:10.1029/2005JD006779.

Dubovik, O., A. Smirnov, B. N. Holben, M. D. King, Y. J. Kaufman, T. F. Eck, and I. Slutsker (2000), Accuracy assessments of aerosol optical properties retrieved from Aerosol Robotic Network (AERONET) Sun and sky radiance measurements, *J. Geophys. Res.*, *105*(D8), 9791–9806.

Dubovik, O., B. N. Holben, T. Lapyonok, A. Sinyuk, M. I. Mishchenko, P. Yang, and I. Slutsker (2002), Non-spherical aerosol retrieval method employing light scattering by spheroids, *Geophys. Res. Lett.*, *29*(10), 1415, doi:10.1029/2001GL014506.

Guerzoni, S., I. Correggiari, and S. Miserocchi (1990), Wind-blown particles from ships and land-based stations in the Mediterranean Sea: A review of trace metal sources, *Water Pollut. Res Rep.*, *20*, 377–386.

Guibert, S., V. Matthias, M. Schulz, J. Boesenberg, R. Eixmann, I. Mattis, G. Pappalardo, M. R. Perrone, N. Spinelli, and G. Vaughan (2005), The vertical distribution of aerosol over Europe—Synthesis of one year of EARLINET aerosol lidar measurements and aerosol transport modelling with LMDzT-INCA, *Atmos. Environ.*, *39*, 2933–2943.

Halthore, R. N., et al. (2005), Intercomparison of shortwave radiative transfer codes and measurements, *J. Geophys. Res.*, *110*, D11206, doi:10.1029/2004JD005293.

Hatzianastassiou, N., B. Katsoulis, and I. Vardavas (2004), Sensitivity analysis of aerosol direct radiative forcing in ultraviolet–visible wavelengths and consequences for the heat budget, *Tellus, Ser. B*, *56*(4), 368–381.

Haywood, J., and O. Boucher (2000), Estimates of the direct and indirect radiative forcing due to tropospheric aerosols: A review, *Rev. Geophys.*, *38*(4), 513–543.

Haywood, J. M., and K. P. Shine (1997), Multi-spectral calculations of the direct radiative forcing of the tropospheric sulphate and soot aerosols using a column model, *Q. J. R. Meteorol. Soc.*, *123*, 1907–1930.

Heymsfield, A. (1975), Cirrus uncinus generating cells and the evolution of cirriform clouds. Part 1: Aircraft observations of the growth of the ice phase, *J. Atmos. Sci.*, *32*, 799–808.

Holben, B. N., et al. (1998), AERONET—A federated instrument network and data archive for aerosol characterization, *Remote Sens. Environ.*, *66*, 1–16.

Kaufman, Y. J., D. Tanré, and O. Boucher (2002), A satellite view of aerosols in the climate system, *Nature*, *419*, 215–223.

King, M. D., Y. J. Kaufman, W. P. Menzel, and D. Tanré (1992), Remote sensing of cloud, aerosol, and water vapor properties from the Moderate Resolution Imaging Spectrometer (MODIS), *IEEE Trans. Geosci. Remote Sens.*, *30*, 1–27.

Lelieveld, J., et al. (2002), Global air pollution crossroads over the Mediterranean, *Science*, *298*, 794–799.

Markowicz, K. M., P. J. Flatau, A. M. Vogelmann, P. K. Quinn, and E. J. Welton (2003), Clear-sky infrared aerosol radiative forcing at the surface and the top of the atmosphere, *Q. J. R. Meteorol. Soc.*, *129*, 2927–2947.

Matthias, V., et al. (2004), Vertical aerosol distribution over Europe: Statistical analysis of Raman lidar data from 10 European Aerosol Research Lidar Network (EARLINET) stations, *J. Geophys. Res.*, *109*, D18201, doi:10.1029/2004JD004638.

Meador, W. E., and W. R. Weaver (1980), Two-stream approximation to radiative transfer in planetary atmospheres: A unified description of existing methods and new improvement, *J. Atmos. Sci.*, *37*, 630–643.

Meloni, D., A. di Sarra, T. Di Iorio, and G. Fiocco (2005), Influence of vertical profile of Saharan dust on the visible direct radiative forcing, *J. Quant. Spectrosc. Radiat. Transfer*, *93*, 397–413.

Nakajima, T., et al. (2003), Significance of direct and indirect radiative forcings of aerosols in the East China Sea region, *J. Geophys. Res.*, *108*(D23), 8658, doi:10.1029/2002JD003261.

Pace, G., A. di Sarra, D. Meloni, S. Piacentino, and P. Chamard (2006), Aerosol optical properties at Lampedusa (central Mediterranean). 1. Influence of transport and identification of different aerosol types, *Atmos. Chem. Phys.*, *6*, 697–713.

Paltridge, G. W., and C. M. R. Platt (1976), *Radiative Processes in Meteorology and Climatology*, Elsevier, New York.

Pavlakis, K. G., D. Hatzidimitriou, C. Matsoukasl, E. Drakakis, N. Hatzianastassiou, and I. Vardavas (2004), Ten-year global distribution of downwelling longwave radiation, *Atmos. Chem. Phys.*, *4*, 127–142.

Perrone, M. R., M. Santese, A. M. Tafuro, B. Holben, and A. Smirnov (2005), Aerosol load characterization over south–east Italy by one year of AERONET Sun-photometer measurements, *Atmos. Res.*, *75*, 111–133.

Ramanathan, V., et al. (2001), Indian Ocean Experiment: An integrated analysis of the climate forcing and effects of the great Indo-Asian haze, *J. Geophys. Res.*, *106*, 28,371–28,398.

Rossow, W. B., and R. A. Schiffer (1999), Advances in understanding clouds from ISCCP, *Bull. Am. Meteorol. Soc.*, *80*(11), 2261–2287.

Rossow, W. B., A. W. Walker, and L. C. Garder (1993), Comparison of ISCCP and other cloud amounts, *J. Clim.*, *6*, 2394–2418.

Russell, P. B., J. M. Livingston, P. Hignett, S. Kinne, J. Wong, A. Chien, R. Bergstrom, P. Durkee, and P. V. Hobbs (1999), Aerosol-induced radiative flux changes off the United States mid-Atlantic coast: Comparison of values calculated from Sun photometer and in situ data with those measured by airborne pyranometer, *J. Geophys. Res.*, *104*, 2289–2307.

Santese, M., F. De Tomasi, and M. R. Perrone (2007), AERONET versus MODIS aerosol parameters at different spatial resolutions over southeast Italy, *J. Geophys. Res.*, *112*, D10214, doi:10.1029/2006JD007742.

Satheesh, S. K. (2002), Aerosol radiative forcing over the tropical Indian Ocean: Modulation by sea-surface winds, *Curr. Sci.*, *82*(3), 310–316.

Seinfeld, J. H., and S. N. Pandis (1998), *Atmospheric Chemistry and Physics: From Air Pollution to Climate Change*, 1235 pp., John Wiley, Hoboken, N. J.

Smolik, J., V. Zdimal, J. Schwartz, M. Lazaridis, V. Harnvanek, K. Eleftheriadis, N. Mihalopoulos, C. Bryant, and I. Colbeck (2003), Size resolved mass concentrations and chemical composition of atmospheric aerosols over the eastern Mediterranean area, measurements of 15 particulate matter, *Atmos. Chem. Phys.*, *3*, 2207–2216.

Takemura, T., T. Nakajima, O. Dubovik, B. N. Holben, and S. Kinne (2002), Single-scattering albedo and radiative forcing of various aerosol species with a global three-dimensional model, *J. Clim.*, *15*(4), 333–352.

Torres, O., P. K. Barthia, J. R. Herman, Z. Ahmad, and J. Gleason (1998), Derivation of aerosol properties from satellite measurements of backscattered ultraviolet radiation: Theoretical basis, *J. Geophys. Res.*, *103*(D14), 17,099–17,110.

Zhou, L., et al. (2003), Comparison of seasonal and spatial variations of albedos from Moderate-Resolution Imaging Spectroradiometer (MODIS) and Common Land Model, *J. Geophys. Res.*, *108*(D15), 4488, doi:10.1029/2002JD003326.

F. De Tomasi, M. R. Perrone, and A. M. Tafuro, Dipartimento di Fisica, Università del Salento, I-73100 Lecce, Italy. (anna.tafuro@le.infn.it)

S. Kinne, Max Planck Institute für Meteorologie, D-20146 Hamburg, Germany.